Early Middle Stone Age personal ornaments from Bizmoune Cave, Essaouira, Morocco

Sehasseh, El Mehdi; Fernandez, Philippe; Kuhn, Steven; Stiner, Mary; Mentzer, Susan; Colarossi, Debra; Clark, Amy; Lanoe, François; Pailes, Matthew; Hoffmann, Dirk; Benson, Alexa; Rhodes, Edward; Benmansour, Moncef; Laissaoui, Abdelmoughit; Ziani, Ismail; Vidal-matutano, Paloma; Morales, Jacob; Djellal, Youssef; Longet, Benoit; Hublin, Jean-jacques

Published in:
Science advances

DOI:
10.1126/sciadv.abi8620

Publication date:
2021

Citation for published version (APA):
Sehasseh, E. M., Fernandez, P., Kuhn, S., Stiner, M., Mentzer, S., Colarossi, D., Clark, A., Lanoe, F., Pailes, M., Hoffmann, D., Benson, A., Rhodes, E., Benmansour, M., Laissaoui, A., Ziani, I., Vidal-matutano, P., Morales, J., Djellal, Y., Longet, B., ... Bouzouggar, A. (2021). Early Middle Stone Age personal ornaments from Bizmoune Cave, Essaouira, Morocco. *Science advances*, *7*(39), Article eabi8620. https://doi.org/10.1126/sciadv.abi8620

Science Advances
AAAS

Supplementary Materials for

Early Middle Stone Age personal ornaments from Bizmoune Cave, Essaouira, Morocco

El Mehdi Sehasseh, Philippe Fernandez*, Steven Kuhn*, Mary Stiner, Susan Mentzer, Debra Colarossi, Amy Clark, François Lanoe, Matthew Pailes, Dirk Hoffmann, Alexa Benson, Edward Rhodes, Moncef Benmansour, Abdelmoughit Laissaoui, Ismail Ziani, Paloma Vidal-Matutano, Jacob Morales, Youssef Djellal, Benoit Longet, Jean-Jacques Hublin, Mohammed Mouhiddine, Fatima-Zohra Rafi, Kayla Beth Worthey, Ismael Sanchez-Morales, Noufel Ghayati, Abdeljalil Bouzouggar*

*Corresponding author. Email: abdeljalil.bouzouggar@insap.ac.ma (A.Bo.); philippe.fernandez@univ-amu.fr (P.F.); skuhn@email.arizona.edu (S.K.)

Published 22 September 2021, *Sci. Adv.* **7**, eabi8620 (2021)
DOI: 10.1126/sciadv.abi8620

This PDF file includes:

Supplementary Text

Geoarchaeology

Bizmoune Cave is broadly divided into two extant chambers. The eastern chamber is the focus of the archaeological excavations. The western chamber is slightly higher than the eastern chamber. The western chamber is larger, but the ceiling is significantly lower relative to the eastern chamber, which renders much of the space inaccessible to human adults in sitting or standing position. There are two main entrances to the cave. The larger, arched southern entrance breaches the east chamber, while a smaller, more tunnel-like western entrance descends down along a bedrock slope into the western chamber. Several small minor entrances along the perimeter of the western chamber have formed from fissures and holes in the bedrock. These entrances are not large enough to permit humans to enter or exit, but may provide access to the site for small animals; however, fecal materials or other evidence of contemporary occupation of the site by wild animals were not observed. Modern modes of sediment deposition into the site include transport through bedrock joints via dripwater, wind, and mass wasting. At present, the only entrance permitting colluvial sediment transport into the site is the tunnel-like western entrance of the western chamber.

The bedrock is strongly bedded, calcareous sedimentary rock of Cretaceous age (*30*). Three main bedrock units are exposed within the cave. The unit that comprises the cave floor contains bedding planes dipping to the southeast and is composed of

dolomite (based on mineralogical analysis, see below). The middle unit is composed of rounded blocks of limestone, with an overall blocky or brecciated structure. The unit that comprises the cave ceiling is composed of a mixture of calcite and dolomite and is more massive in appearance, although outside of the cave the unit shows horizontal bedding. The joint pattern in this uppermost unit is both horizontal and vertical (two planes at 60/40), yielding large, rhombohedral blocks of roof fall. Outside of the cave, the bedding in this unit is near horizontal, and this seems to have extended to the area within the cave, as the ceiling is generally flat, with a slight dip to the southeast. This unit is also silicified, as evidenced by its conchoidal fracture and minor silica visible in FTIR spectra (see below). Rocks from this unit may have been exploited as a raw material source.

The middle unit exhibits a wedge shape within the cave and has an internal fabric that is consistent with a fault breccia. A thin (20-30 cm) band of soft material, white to yellow in color, is present in some areas at the contact between the lower and middle units. This band is highly erodible, with a texture similar to chalk, and its mechanical weathering (along the suspected fault plane) as well as the slightly higher solubility of the limestone in this unit compared to the over- and underlying dolomite may have accelerated the phreatic activity that formed the chambers.

The stratigraphy of the archaeological sequence

The stratigraphic descriptions below reflect lithostratigraphic and micromorphological descriptions supported by archaeological data. The unit descriptions can be summarized as follows :

1, 32 cm thick. Poorly consolidated, grey (10GY 4/0) ashy silt and this layer can be divided into three sub layers:

1a, 18 cm thick. Grey (10GY 4/0) ashy silt. Neolithic artifacts.

1b, 9 cm thick. Dark grey ashy silt (7.5YR 4/1) and less disturbed than 1a. A sparse layer of small angular gravel (<5 cm) appears at the base of this layer. LSA (Iberomaurusian) artifacts.

1c, ~5 cm thick. Poorly consolidated reddish grey silt (5YR 5/2) thicker outside the cave (5 cm). LSA (Iberomaurusian) artifacts.

2, ~18 cm thick. Composed of a series of two carbonate crusts and a cemented layer in between. This layer could be divided into three sub layers:

2a, 1 cm thick. A well developed and sometimes cracked carbonate crust in the cave entrance (N-O-P7 to 9 squares). LSA (Iberomaurusian) artifacts.

2b, 15 cm thick. A cemented pale brown (10Y 7/4) sandy silt more visible inside and near the cave entrance (N-O-P7 to 9 squares) but very well defined in the middle of the cave entrance just below the dripline. A subdivision of this layer (2b') is very localized in the site. MSA (Aterian) artifacts.

2c, 1 to 2 cm thick. A carbonate crust visible only in the center of the cave.

3, 50 cm thick. A cemented pale brown sandy silt (5Y 5/6), containing more-or-less angular limestone pebbles. Thin and discontinuous carbonate crusts divide this layer in three main units, 3a, 3b, and 3 *inferior*. MSA (Aterian) artifacts.

4, > 150 cm thick. A cemented dark brown silt. Although charcoal and ash are common in thin sections there are no intact combustion features, probably due to small-scale bioturbation. A series of phosphatic crusts (4b) divide this into sub layers.

4a, ~50 cm thick. A highly cemented silt light gray (2.5 YG 8/1). MSA/Aterian artifacts.

4b, 1~2 cm layer of discontinuous phosphatic crusts.

4c, ~50 to 100 cm thick is dark gray silt (N 4/0) and not as consolidated as 4a. MSA (Aterian) artifacts.

4c', 1~2 cm thick. An isolated carbonate crust within layer 4c close to the current cave mouth, squares 07 and N7.

Observations from Layer 4

Twenty-two thin sections produced from Layer 4 were analyzed for this study. Geogenic components of the sediment include angular to well-rounded clasts of bedrock, sand- and silt-sized grains of quartz and feldspar, and aggregates of soil. The vast majority of bedrock fragments in this unit are composed of dolomite and are thus sourced from either the floor or ceiling units of the cave. Soil aggregates are coarse sand to gravel sized, and reddish in color. They are generally similar to the modern soil that has entered the site via colluviation into the western entrance, although the latter is richer in organic material and is more brown in color. Biogenic components include snail shell and rare fragments of coprolite. Additionally, a clay-rich soil component may have been transported into the site by burrowing insects for the construction of pupal cavities.

Anthropogenic materials are abundant in the Layer 4 sediment (Fig. 2). Fragments of bone and teeth are common, and both exhibit variability in weathering and changes in optical properties and FTIR spectra that indicate heating (*31*). Wood ashes and sand-sized aggregated of cemented wood ashes mixed with charcoal are also present. Microcharcoal is the most abundant anthropogenic component, comprising ~10% volume of the fine sediment in places. Fat-derived char is less common but also present. Rare anthropogenic components include sixteen sand-sized ochre fragments

that were observed in thin section using oblique incident light (with identification confirmed using elemental analysis).

The abundance of charcoal fragments and burned bone indicate that controlled use of fire was a common practice at the site during the formation of Layer 4. Only one intact combustion feature was identified during excavation and sampled for micromorphological analysis. This feature was constructed on top of the bedrock just outside of the modern dripline of the cave. The main components are illustrated in Fig. S1. Although Layer 4 exhibits broad vertical variation in the relative abundance of bedrock clasts and anthropogenic materials, microstratigraphy or preserved surfaces were not observed. Post-depositional processes that have homogenized the sediments include the formation of secondary carbonate within cracks and channels, and bioturbation by insects. Shell beads were not encountered in thin section, but the observation of snail shell fragments indicates that the burial conditions were favorable for the preservation of calcite throughout Layer 4, as well as within overlying layers.

Additional observations

Although the upper layers of the site are not the focus of this paper, micromorphological observations suggest that the initiation of flowstone formation at the top of layer 4 marked a shift in the nature of the sediment at the site. Layer 4 deposits are rich in anthropogenic materials, clastic material and allochthonous soil aggregates. Sediments in Layer 3 and above show a more autochthonous, fine-grained chemical mode of sedimentation with high moisture. The flowstones that cap layer 4 are laminated and contain detrital material (Fig. S2). In several areas it appears that the flowstones have formed on top of one or more erosional surfaces.

Faunal remains

Preservation of fauna varies within the Bizmoune Cave sequence. Faunal remains from all MSA contexts are covered by a hard, thick calcitic crust which makes taxonomic identification and taphonomic study difficult. The seven faunal units (F7-F1) are presented following the stratigraphy of the cave and the dated contexts, including cultural phases, related to marine isotope stages and paleotemperatures (*32*). The presence/absence of particular taxa is indicated for each faunal unit, along with Number of Identified Specimens (NISP) (Fig. S3). Instances in which a species is missing from a layer but occurs in the surrounding layers probably result from taphonomic bias, poor sampling or bad preservation of the fossil remains.

More precise taxonomic determination of some species is ongoing due to the scarcity and the poor state of the remains in some layers. Among the Antilopini of Bizmoune we identified *Gazella* sp., which is represented throughout the entire sequence except F4. These remains could correspond to one or more forms of *Gazella* that are morphometrically different from *Gazella* cf. *atlantica,* which has only been found in the Early MSA and the MSA of Bizmoune (F7) and seems to disappear in the Early Holocene (*33*). Alcelaphini are represented by *Alcelaphus buselaphus* (F7, F5, F3, F1) and *Connochaetes* cf. *taurinus prognu* in Faunal Unit 7. Hippotragini only occur with *Hippotragus* cf. *equinus* (F7) and *Oryx* cf. *dammah* (F1). They are rare in north African archaeological sites, but living *O. dammah* were mentioned in the extreme south of Morocco during the first half of the 20th century and few remains of this species were discovered in the Neolithic layers of Kaf-Taht-el Ghar (*34*). *Bos primigenius* is present across the earlier and later parts of the sequence (F7 to F5, F1). Among the Suidae, remains of *Phacochoerus africanus* are present in F7, F6, and F1. These are easily distinguished from remains of the wild boar, *Sus scrofa* which is only

present in the Neolithic of Bizmoune (F2, F1). The Equidae are currently being analysed, with *Equus* sp. (F7 to F3, except F4) and *Equus* cf. *mauritanicus* (F7) identified so far. They are different from the true caballine wild species *E. algericus* recognized in other North African sites from the Holocene to the MSA/Aterian (*35-37*). The Rhinocerotidae are represented in F7 and F6 by *Stephanorhinus* cf. *hemitoechus* (also known as *Dicerorhinus hemitoechus*) and in F1 by *Ceratotherium simum*. These two rhinos were the only representatives of the group during the Upper Pleistocene in Morocco, and they are very rare in archaeological sites. *S. hemitoechus* dispersed into in Morocco (*38*) around the Middle/Upper Pleistocene boundary, along with other mammals of Eurasiatic origin, probably through the Strait of Gibraltar or from the east along the southern Mediterranean coastline (*39*). This species might have become extinct at the end of the Aterian period when *C. simum* reappeared (*40*).

The first appearance in Bizmoune of *Ammotragus lervia*, *S. scrofa*, *Megaceroides algericus* and *Panthera* cf. *pardus* is in F2, at base of the early Neolithic, although all these taxa are represented at older sites in Morocco. The Barbary sheep (*A. lervia*) is often very abundant in late-Pleistocene Late Stone Age (LSA)/Iberomaurusian and Holocene sites in Maghreb. The wild boar (*S. scrofa*) appeared mainly at the end of the Late Pleistocene in North Africa (*40*, *41*). The latest dated occurrence in the Maghreb of the endemic *M. algericus* is in the Neolithic layers (F2) of Bizmoune (*42*). The genus *Panthera* is relatively rare in Pleistocene deposits of the Maghreb but *Panthera* cf. *pardus* could be present up through the "late Cardial - Neolithic recent" in other sites (*43*). To date, the few remains of this feline and those of Canidae (probably *Vulpes*/*Canis*) from Bizmoune all come from Neolithic layers (F2 and F1). Nevertheless, some fragments of carnivore coproliths were also identified in F7 and F5. The scarcity of the carnivores in all the layers of Bizmoune indicates that the

faunas are mainly anthropogenic accumulations, an inference further supported by the frequencies of cutmarks and traces of burning. The remains of *Capra* cf. *hircus* indicate that goat was already domesticated in F1, but the remains of the Bovini do not belong to domesticated cattle *B. primgenius f. taurus*. This suggests that the Neolithic groups may have used domestic goats but also hunted/scavenged aurochs, wild boar, and the other wild species in F1 (*i.e. Gazella* sp., *A. lervia*, *A. buselaphus*, *Oryx* cf. *dammah*, *P. africanus*).

Alongside the exploitation of large mammals, fragmented remains of ostrich eggs (*Struthio* sp.) are present throughout the sequence (F7 to F1). Remains of tortoise (*Testudo* sp.) are also widespread (all units except in F5, F4). Lagomorph remains are present in F7 (*Lepus capensis* and *Oryctolagus* sp.) and in the late Neolithic F1 (*Lepus/Oryctolagus* F1). This may indicate relatively broad-based subsistence strategies, including small terrestrial game, in the earliest phases of the sequence.

Anthracological remains

A total of 376 charcoal fragments from layers 3inf and 4c have been analysed (Table S1). Remains of *Juniperus/Tetraclinis* (46.39%) are common in layer 4c, followed by *A. spinosa* (38.66%), Angiosperms (10.82%) and other species including *Pistacia* sp. (mastic or terebinth) (2.06%) and *Salix/Populus* (2.06%).

The anthracological data from layer 4c indicate open plant formations of juniper and/or *araar* together with the presence of argan. The climate would have been marked by sub-arid (mean annual precipitation or MAP <200 mm) or semi-arid (MAP between 200-350 mm) conditions (*16*, *17*, *44*).

Stone tools

Most of the stone artifacts from Bizmoune, including layer 4c, were made of flint. At least four varieties of flint are represented in the assemblage from layer 4c. These mostly derived from Cretaceous bedrock contexts. All these materials have a dusky colour varying from brown to dark brown red or black. Non-flint raw materials identified in layer 4c include limestone and silicified limestone. Dolerite, quartz, gabbro and quartzite are less common.

The artifact assemblage from layer 4 shows typical Aterian characteristics throughout, including small Levallois cores, a variety of side- and end-scrapers, and of course tanged (pedunculate) artifacts along with a small number of bifacial foliates. The tanged tools are mostly asymmetrical (Fig. 3) in the tang or the body. However, the asymmetry of the body could be the result of differential reduction of the lateral and/or distal margins over the use-life of the artifact, as suggested by abrupt and/or stepped retouch. The assemblages from 4c also contains a number of cobble tools made from volcanic rocks that were apparently used to pound and grind other materials. Some, but not all of these are stained with red ochre.

The dominant mode of flake production in layer 4c at Bizmoune cave is centripetal Levallois. However, blades are present in smaller numbers throughout the layer. In a random sample of artifacts from the 2017 and 2018 seasons, around 5.7% of unmodified blanks can be classified as blades, and three of 31 cores are single platform blade cores. The frequency of blades used as blanks for retouched tools (9.7%) is even higher. If anything, the number of blades within each category is underestimated, as it was impossible to assign the original blank form to many broken specimens, and to some heavily modified tools.

Use-wear

A total of ten tanged tools of different sizes were examined for traces of use-wear. Evidence of hafting was observed on all of them, including intentional proximal thinning, removal of the bulbs and small scars caused by contact with the haft. Similar modification was also observed on some scrapers. Most of the sidescrapers examined display macroscopic wear such as edge rounding and scars with well-developed extension, showing evidence of working hard materials.

Only three of the tanged tools are complete. Two of them showed impact damage and one had well-developed macro-scars on the ventral face of the distal part, indicating the scraping hard materials. The remaining tanged tools (n=7) are broken and missing their distal segments including the thickest parts, which would indicate their use in activities involving high levels of force or impact. Three bladelets were also examined. Two of them show rounding on their tips indicating their probable use for piercing.

The shell beads

Shell beads from MSA and Middle Paleolithic contexts are a topic of continuing interest in both Africa and the Levant (*45, 46*). We adopted the term *Tritia gibbosula* Risso 1826 rather than *Nassarius gibbosulus* following the World Register of Marine Species (WoRMS, http://www.marinespecies.org/) for current nomenclature (*22, 47-48)*. Many archaeological publications use the synonymous term *Nassarius gibbosulus.*

The *Tritia* and C*olumbella* shells from Bizmoune show a wide range of damage and modifications, including beach wear, evidence for human use and modification (chipping, polishes around the aperture), traces of red pigment, and probably post-depositional damage (Table S2, Fig. 6, 7). Most of the beads were found in the

northernmost part of the excavated area where the trench is deepest (Fig. 4). The density of ornaments is highest in the lower part of layer 4c, lower in elevation than the dated speleothem, 4c' (Fig. 4). Compared with a substantial database (n=358) of *T. gibbosula*, *N. circumcinctus* and *C. rustica*, a bivariate analysis (length/width) indicates that *T. gibbosula* from Bizmoune are relatively large compared with the most important documented Middle Stone Age shell ornament samples for North Africa (e.g. Taforalt, Ifri n' Amar, Rhafas, Djebbana, Contrebandiers) and the Levant (Skhul) as well as from modern samples (Fig. S4). The size differences among samples certainly reflect the plasticity and adaptation of the various populations of *Tritia* to their local environments.

Uranium series dating, Max Planck Institute for Evolutionary Anthropology

Four samples of flowstone were dated at the Max Planck Institute (MPI) for Evolutionary Anthropology, Leipzig Germany (Table S3).

At the Max Planck Institute, all ratios are activity ratios. Analytical errors are at 95 % confidence level. Activity ratios are calculated from isotope concentration ratios using decay constants (*49*) (λ238), (50) (λ234 and λ230) and (*51*) (λ232). The degree of detrital ^{230}Th contamination is indicated by the measured ^{230}Th/^{232}Th activity ratio and corrections were calculated using a ^{238}U/^{232}Th activity ratio of 0.8 ± 0.4 and assuming secular equilibrium of the ^{238}U decay chain in the detritus.

Uranium series dating, CNESTEN

Seven samples at National Center for the Techniques Science and Nuclear Energy (CNESTEN), Rabat Morocco (Table S4). 2-sigma confidence intervals are given for measured quantities and ages. The uranium-series disequilibrium dating method is based on the growth of ^{230}Th from the disintegration of its progenitors, namely ^{234}U

and ^{238}U. Assuming that initially there are only ^{234}U and ^{238}U in the sample. The activity of ^{230}Th at a time *t* is given by the following equation derived from Bateman equations:

$$^{230}Th = {}^{238}U \cdot (1 - e^{-\lambda_{230} \cdot t}) + ({}^{234}U - {}^{238}U) \cdot \left(\frac{\lambda_{230}}{\lambda_{230} - \lambda_{234}} \right) \cdot \left(1 - e^{-(\lambda_{230} - \lambda_{234})t}\right)$$

The age *t* is determined either by a graphical method using the ^{234}U/^{238}U *vs* ^{230}Th/^{234}U isochrones, obtained for different ages, or an iterative method based on the Newton Raphson algorithm. The second approach was applied in this study. It's assumed that at material formation, the thorium content is zero and uranium and thorium have not been moved into or out of the dated material. This is called a **closed system** which is particularly relevant to applying U-series dating to material with carbonates as human and animal remains (bones and teeth) and **speleothems.**

Prior to radiochemical separation, samples were roughly cleaned to remove any adherent material that does not belong to the sample surface by using more or less abrasive tools such as brush, milling machine and sandpaper. The cleaned sample was then washed with bi-distilled water. For determination of U and Th isotopes (^{234}U, ^{238}U and ^{230}Th)– aliquots of 1 - 2 g of each sample was totally digested with concentrated nitric acid after spiking with known amounts of ^{232}U and ^{229}Th yield tracers, respectively. The acid digest was repeatedly evaporated with concentrated HNO_3-H_2O_2 and finally dissolved in 20 ml of 8M HNO_3. U and Th were separated by liquid-liquid extraction using the organic solvent TBP (Tri-butyl phosphate), and then purified using an anion-exchange resin (Dowex1-X8, Cl^- form) to remove traces of resolution-degrading elements that interfere in alpha particle spectra. U and Th

isotopes were electrodeposited on stainless steel discs and the resulting alpha sources were analysed by alpha-ray spectrometry using silicon surface barrier detectors (EG&G) coupled to a PC running Maestro^{TM} data acquisition software.

Before dating the speleothem (4c'), one of the co-authors (F-Z R) made a thin section on the flowstone to determine whether the crust is suitable for this technique and to assist the lab in sampling it properly. Fig. 8 shows an image of the thin section and the area sampled. The thin section shows dense, micritic carbonate with some detrital material incorporated into the carbonate just above the contact but outside of the sampling area. Ideally, a flowstone for dating should be sparitic, but none of the flowstones at Bizmoune are sparitic. In absence of primary spar crystals, one would prefer a flowstone that is dense, that does not show signs of recrystallization, and that does not contain fragments of older carbonate. This flowstone meets all of these criteria. ^{232}Th activities in all samples were below the Minimum Detectable Activity (MDA) about 0.16 Bq/kg corresponding to a Minimum Detectable Concentration of 39.27 ng/g and leading to ^{230}Th/^{232}Th activity ratios in Table S4 greater than 20. The presence of detrital material in the samples could be deemed as insignificant for thorium isotopic ratios above 20 and thus no correction on the calculated ages is required (*52, 53)* (Table S4).

The conventional age, t, is calculated by solving numerically (Newton-Raphson algorithm) the following equation:

$$\frac{^{230}\mathrm{Th}}{^{234}\mathrm{U}} = \frac{1-e^{-\lambda 230.t}}{\frac{^{234}\mathrm{U}}{^{238}\mathrm{U}}} + \left(1-\frac{1}{\frac{^{234}\mathrm{U}}{^{238}\mathrm{U}}}\right)\left(\frac{\lambda_{230}}{\lambda_{230}-\lambda_{234}}\right)\left(1-e^{-(\lambda 230-\lambda 234).t}\right) \quad (1)$$

We used the following decay constants of ^{230}Th and ^{234}U :

- λ_{230} : $9.1577.10^{-6}$ a^{-1} for ^{230}Th

- λ_{234} : $2.826.10^{-6}$ a^{-1} for ^{234}U

Both uncertainties on $^{230}Th/^{234}U$ and $^{234}U/^{238}U$ were considered for the calculation of uncertainties on the ages. The lower and upper limits of the age were estimated by using the minimal and maximal values of $^{230}Th/^{234}U$ and $^{234}U/^{238}U$ in the above equation (1):

the lower limit is obtained using: $\frac{^{230}Th}{^{234}U} - u\left(\frac{^{230}Th}{^{234}U}\right)$ *and* $\frac{^{234}U}{^{238}U} + u\left(\frac{^{234}U}{^{238}U}\right)$

the upper limit is obtained using: $\frac{^{230}Th}{^{234}U} + u\left(\frac{^{230}Th}{^{234}U}\right)$ *and* $\frac{^{234}U}{^{238}U} - u\left(\frac{^{234}U}{^{238}U}\right)$

Where $u(^{230}Th/^{234}U)$ and $u(^{234}U/^{238}U^{238})$ are the uncertainties on radionuclide activity ratios $^{230}Th/^{234}U$ and $^{234}U/^{238}U$ respectively at 2-sigma confidence interval.

We present the activity ratios of $^{230}Th/^{234}U$ and $^{234}U/^{238}U$ with their respective uncertainties as well as the ages and their maximum and minimum uncertainties in ka (Table S4). These uncertainties on the ages were calculated directly from the uncertainties on the activity ratios of $^{230}Th/^{234}U$ and $^{234}U/^{238}U$ and by inserting the above terms (lower limit and upper limit) in the equation 1.

<u>OSL Dating, Max Planck Institute for Evolutionary Anthropology</u>

Eight samples were collected from the excavation site in Bizmoune Cave, by hammering metal tubes into the exposed wall of the excavation pit. Samples were transported to the laboratory in light-tight packaging and all laboratory preparation was completed under subdued red-light conditions. The sample from the outer ends of the tubes was used to measure the modern burial and saturated water content, and for high resolution gamma spectrometry measurements. The luminescence sample was wet sieved, and the 90-250 µm grain size fraction treated with hydrochloric acid (HCl) and hydrogen peroxide (H_2O_2) to remove carbonate and organic material,

respectively. Pure quartz was separated from the bulk sample using sodium polytungstate (SPT) at a density of 2.62 and 2.70 g/cm^3. The quartz fraction was etched with 40% hydrofluoric (HF) acid for 45 min to remove the alpha-irradiated surface of the grains, in addition to any remaining feldspar grains

All luminescence measurements were made on an automated Riso TL/OSL DA-20 reader with optical stimulation for single grain measurements using the 10 mW green laser (532 nm). Detection in the UV region was made by an EMI 9235QB PMT filtered by a 7.5 mm Hoya U-340 glass filter. Laboratory irradiations were made using a ^{90}Sr/^{90}Y beta source, with a beta dose rate of 0.116 Gy/s. The luminescence signal was measured using a SAR protocol with a regeneration dose preheat of 220 °C for 10s and a test dose preheat of 160 °C for 10s.The suitability of the protocol for single grain measurements was tested by a dose recovery test on individual grains of quartz for sample L-EVA-1829, which produced a measured/given dose ratio of 1.05±0.02 (n=116, OD=5%). Dose response curves (DRCs) were fit with a single saturating exponential (SSE) function. Single grain equivalent dose (D_e) values were calculated by integrating the luminescence signals from the initial 0.15s of the decay curve and subtracting a late background from the last 0.3s of the decay curve. Individual equivalent dose values were only accepted if (i) the recycling ratio was within 10% of unity, (ii) recuperation was less than 5% of the natural signal, (iii) the error on the test dose signal was less than 3 standard deviations, and (iv) the uncertainty on the test dose was less than 10%. Potential feldspar contamination was monitored using the OSL/IR depletion ratio (*54*).

The samples are well-bleached, with typical overdispersion values of 23-30% (except sample L-EVA-1826, OD=46%), and the central age model (CAM) (*55*) was used to calculate the ages. The equivalent dose (D_e) measurements and dose rate calculations

are summarised in Table S5. The environmental dose rate was calculated using high resolution gamma spectrometry (HRGS). The total dose rate for each sample was calculated using the Dose Rate and Age Calculator (*56*). Water content corrections were made using the measured water content at the time of sampling.

OSL Dating, Sheffield University

Eleven samples were dated in two batches, using a single grain approach incorporating a SAR protocol that is very similar to that used at MPI, but with a small number of differences. Results are summarized in Table S6. Samples were collected by the archaeology team members using opaque PVC tubes hammered horizontally into sediments exposed in section in the trench wall. Quartz grains of 180-212μm were extracted using a combination of wet and dry sieving. This was followed by a treatment with dilute HCl and H_2O_2, HF treatment (40%) for 40 minutes, and a density treatment at 2.70 $g.cm^{-3}$. After copius rinsing, and drying, grains were mounted in Risø single grain holders. OSL measurements were made on a DASH TL-DA-20 automated Risø unit using an identical green laser to that used at MPI, detected using 2.5mm Hoya U340 filter with a PDM9107Q-CP-TTL-02photomultiplier. Samples were preheated at 260°C for 10s for natural and regenerative dose points, and 220°C for 10s for the sensitivity correction measurement.

For the Sheffield samples, analysis for the single grain populations was similar to that described for K-feldspar grains (*57*), which is a procedure based on the CAM of (*55*), following rejection of grains using an OD value of 15%. Several samples measured in Sheffield displayed populations of grains with lower equivalent dose values, and significantly lower sensitivities. These are tentatively interpreted as intrusive grains from a younger sterile horizon and were excluded from the age analysis. Dose rates

for the 11 Sheffield samples were calculated based on ICP-MS for U and Th and ICP-OES for potassium, using material extracted from the ends of the sample collection tubes, plus a small cosmic dose rate contribution. A uniform value of water content of 15 ± 5% was used for these ages; we note that this is similar to the measured values used for the MPI samples.

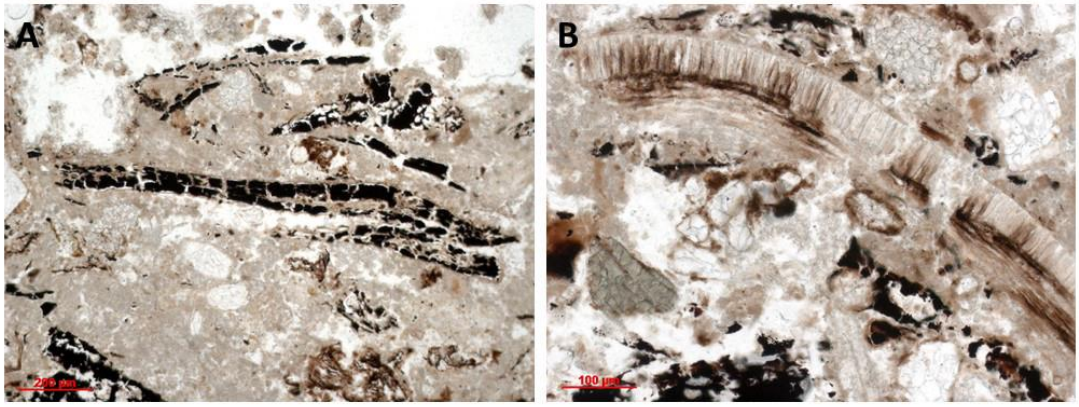

Fig. S1: Contents of the intact combustion feature: A, Charcoal fragments in a matrix of partially recrystallized wood ashes; B, fragment of a seed.

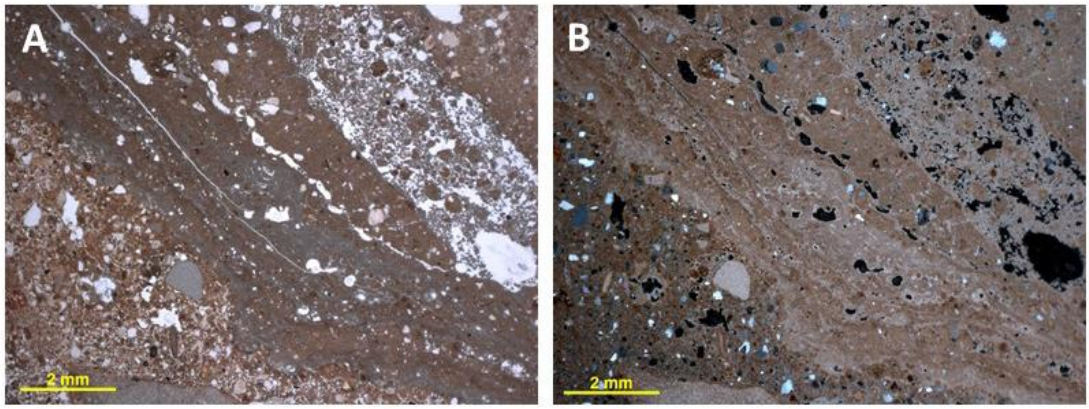

Fig. S2: Flowstone in thin section: A, View of one of the dated flowstones with multiple discrete layers of calcite. The sediment above the flowstone is bioturbated, and the flowstone has served as a barrier to movement of sediment downwards; B, Same view as A., cross-polarized light.

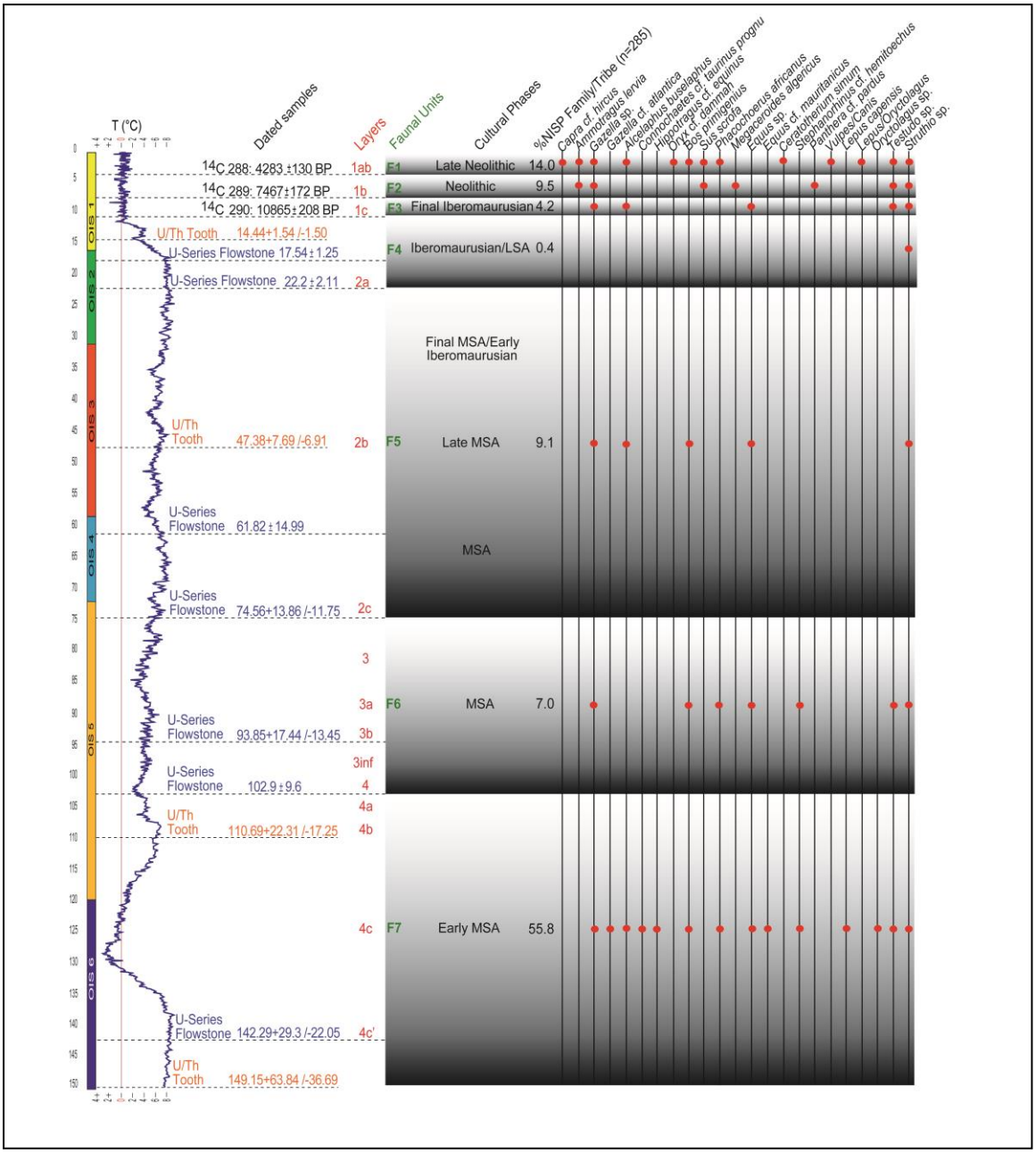

Fig. S3: Summary of faunal, archaeological and chronological frameworks of Bizmoune Cave showing occurrence of major taxa in different stratigraphic units. Marine isotope stages and paleotemperatures from *32*.

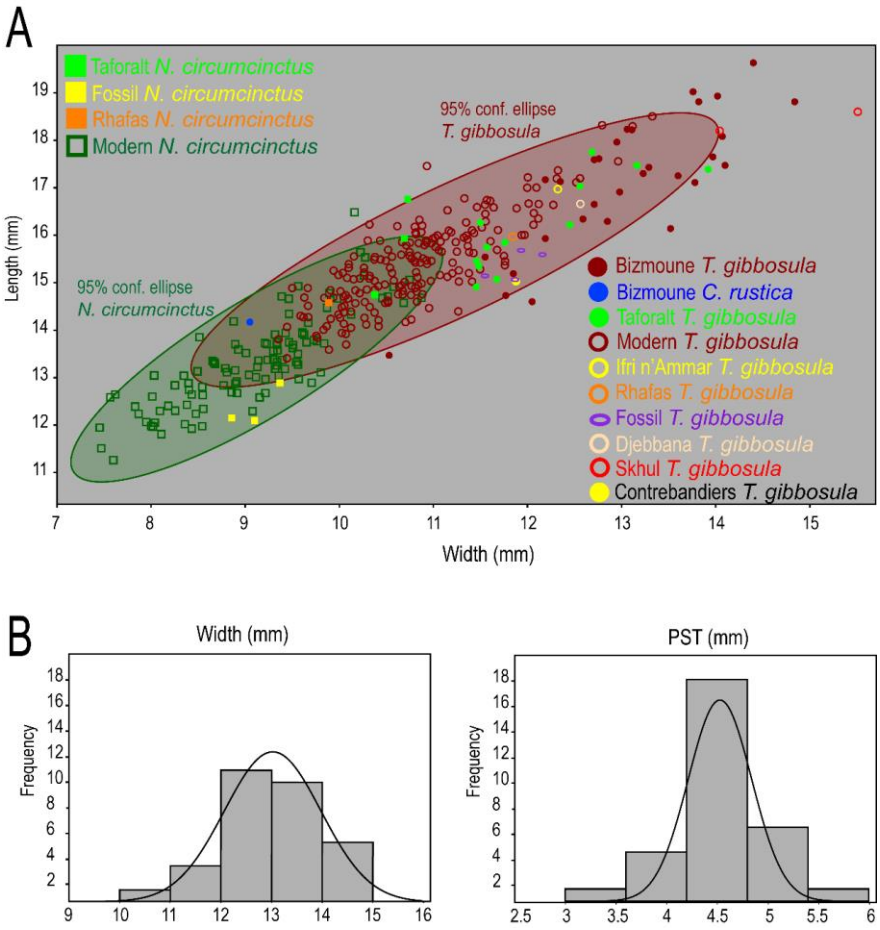

Fig. S4. A. Comparison of the sizes of *Tritia* shells from Bizmoune Cave with other MSA/Middle Paleolithic sites in North Africa and the Levant. B. Distributions of width and parietal shield thickness (PST) of *Tritia gibbosula* shells from Bizmoune Cave. (Data from sites other than Bizmoune from *29*).

	Layer 3inf		Layer 4c	
Taxon	**N**	**%**	**N**	**%**
Juniperus/Tetraclinus	118	64.8	90	46.4
Argania spinosa	47	25.8	75	38.7
Salix/Populus	5	2.8	4	2.06
Pistacia sp.	--	--	4	2.06
Angiosperms	12	6.6	22	10.8
Total	182	100	194	100

Table S1. Taxonomic summary of charcoal fragments from layers 3inf and 4c at Bizmoune Cave.

ID	Species	Length (mm)	Width (mm)	PST* (mm)	Shells or sand inside	Post - depositional alteration	Polish on perforation edge	Polish on the apex
6191	*Tritia gibbosula*	15.19	11.85	4.82	Possible	Yes	Yes	No
6316	*Tritia gibbosula*	16.65	12.71	4.64	No	No	No	Yes
6336	*Tritia gibbosula*	16.29	12.85	4.46	No	Yes	Yes	No
6419	*Tritia gibbosula*	18.81	14.84	5.54	No	Yes	No	No
6448a	*Tritia gibbosula*	18.23	13.06	5.21	No	Yes	Yes	No
6448b	*Tritia gibbosula*	17.59	12.71	4.38	No	No	No	No
6501	*Tritia gibbosula*	16.34	12.59	4.21	No	Possible	No	No
6625	*Tritia gibbosula*	15.93	12.19	4.27	No	Yes	Yes	Yes
6914	*Tritia gibbosula*	19.63	14.4	4.71	No	No	Yes	No
7460	*Tritia gibbosula*	16.14	13.52	4.17	No	No	Yes	No
7586	*Tritia gibbosula*	17.17	12.19	4.4	No	Yes	Yes	No
7773	*Tritia gibbosula*	14.73	11.77	4.61	No	Yes	Yes	No
7870	*Collumbella rustica*	14.17	9.05	_	No	Yes	Yes	No
8115	*Tritia gibbosula*	14.6	12.05	4.08	No	Yes	No	No
8195	*Tritia gibbosula*	13.47	10.53	3.03	No	Yes	Yes	No
8501	*Tritia gibbosula*	16.91	12.98	4.41	No	No	Yes	Yes
8523	*Tritia gibbosula*	18.08	14.07	4.74	Possible	Possible	No	No
8693	*Tritia gibbosula*	19.02	13.76	4.85	No	No	Yes	No
8694	*Tritia gibbosula*	17.43	13.29	4.86	No	No	Yes	No
8884	*Tritia gibbosula*	18.81	13.82	4.54	No	No	No	No
9369	*Tritia gibbosula*	17.11	13.78	4.55	No	Yes	Yes	No
9539	*Tritia gibbosula*	_	_	_	No	No	_	Yes
9574	*Tritia gibbosula*	18.93	14.02	4.67	No	No	Yes	No
9596a	*Tritia gibbosula*	18.22	13.11	4.51	No	Yes	Yes	No

9596b	*Tritia gibbosula*	15.54	11.55	4.12	No	Yes	Yes	No
9670	*Tritia gibbosula*	_	12.46	4.27	No	No	Yes	No
9701	*Tritia gibbosula*	17.13	12.35	4.25	No	Yes	Yes	Yes
9791	*Tritia gibbosula*	17.3	13.23	4.18	No	No	Yes	No
9898a	*Tritia gibbosula*	17.65	13.97	5.03	No	No	Yes	No
9898b	*Tritia gibbosula*	17.47	14.1	5.03	No	No	Yes	Yes
10141	*Tritia gibbosula*	17.61	12.76	4.49	No	Yes	Yes	No
10233	*Tritia gibbosula*	17.96	12.95	4.7	No	No	Yes	Yes
10276	*Tritia gibbosula*	17.25	13.6	4.53	No	Yes	Yes	No

ID	Species	Ventral facet	Polish and/or striations on lateral face	Pigment traces	Chipping around aperture	Dorsal perforation	Other perforation	Perforation shape
6191	*Tritia gibbosula*	Yes	Yes	Yes	Yes	Yes	No	Ellipsoid
6316	*Tritia gibbosula*	Yes	No	Yes	Partly	Yes	No	Ellipsoid
6336	*Tritia gibbosula*	No	No	No	Possible	Yes	No	Ellipsoid
6419	*Tritia gibbosula*	No	No	Yes	No	Yes	No	Ellipsoid
6448a	*Tritia gibbosula*	No	No	Yes	Partly	Yes	No	Ellipsoid
6448b	*Tritia gibbosula*	No	No	Yes	Partly	Yes	No	Ellipsoid
6501	*Tritia gibbosula*	No	No	No	Yes	Yes	No	Ellipsoid
6625	*Tritia gibbosula*	Yes	No	No	Yes	Yes	No	Circular
6914	*Tritia gibbosula*	Yes	Yes	Yes	Yes	Yes	No	Ellipsoid
7460	*Tritia gibbosula*	No	No	Yes	Yes	Yes	No	Ellipsoid
7586	*Tritia gibbosula*	Yes	No	Yes	Partly	Yes	No	Ellipsoid
7773	*Tritia gibbosula*	Yes	Yes	Yes	Yes	Yes	No	Ellipsoid
7870	*Collumbella rustica*	No	No	Yes	Yes	Yes	No	Rectangular?

8115	*Tritia gibbosula*	No	No	Yes	No	Yes	No	---
8195	*Tritia gibbosula*	No	No	Yes	Partly	Yes	Yes	Ellipsoid
8501	*Tritia gibbosula*	Yes	No	No	Possible	Yes	No	Ellipsoid
8523	*Tritia gibbosula*	No	No	No	No	Yes	No	Ellipsoid
8693	*Tritia gibbosula*	No	No	Yes	Partly	Yes	No	Ellipsoid
8694	*Tritia gibbosula*	Yes	No	No	Yes	Yes	No	Ellipsoid
8884	*Tritia gibbosula*	No	No	No	Yes	Yes	No	Rectangular
9369	*Tritia gibbosula*	Yes	No	Yes	Partly	Yes	No	Ellipsoid
9539	*Tritia gibbosula*	Possible	_	No	_	Yes	No	Ellipsoid
9574	*Tritia gibbosula*	Possible	No	Yes	Possible	Yes	Yes	No
9596a	*Tritia gibbosula*	No	No	No	Possible	Yes	No	Elipsoid
9596b	*Tritia gibbosula*	No	Possible	Yes	No	Yes	No	Ellipsoid
9670	*Tritia gibbosula*	Yes	Yes	Yes	Partly	Yes	No	Ellipsoid
9701	*Tritia gibbosula*	Yes	No	Yes	Yes	Yes	No	Ellipsoid
9791	*Tritia gibbosula*	Yes	Yes	No	Yes	Yes	No	Rectangular
9898a	*Tritia gibbosula*	No	No	Yes	Yes	Yes	No	Triangular
9898b	*Tritia gibbosula*	Yes	No	Yes	Partly	Yes	No	Ellipsoid
10141	*Tritia gibbosula*	No	No	Yes	Yes	Yes	No	Circular
10233	*Tritia gibbosula*	Yes	Possible	Yes	No	Yes	No	Elipsoid
10276	*Tritia gibbosula*	Yes	Yes	No	Partly	Yes	No	Ellipsoid

*Parietal Shield Thickness

Table S2. Summary of observations including morphology, modification, and damage to shell ornaments from Layer 4c at Bizmoune cave.

											Measured ratios			
Lab ID	**Layer**	**Dated material**	**^{238}U (ng/g)**	**±**	**s (ng/g)**	**±**	**[$^{230}Th/^{232}Th$] activity ratio**	**±**	**($^{232}Th/^{238}U$) activity ratio**	**±**	**($^{230}Th/^{238}U$) activity ratio**	**±**	**($^{234}U/^{238}U$) activity ratio**	**±**
UEVA246	2a	flowstone	521.7	5.5	87.62	0.91	4.50	0.03	5.513E-02	1.346E-04	0.2475	0.0019	1.1452	0.0023
UEVA249	2a	flowstone	632.5	8.8	61.80	0.86	5.96	0.06	3.207E-02	7.060E-05	0.1907	0.0020	1.1343	0.0022
UEVA247	2c	flowstone	207.3	4.2	223.74	4.29	1.88	0.04	3.542E-01	1.023E-03	0.6627	0.0130	1.1484	0.0042
UEVA248	4a	flowstone	380.0	3.2	343.87	2.80	2.78	0.01	2.971E-01	8.319E-04	0.8237	0.0047	1.1741	0.0025

		uncorrected results				Corrected ratios			
Lab ID	**Layer**	**Age (ka)**	**±**	**($^{234}U/^{238}U)_{initial}$ activity ratio**	**±**	**($^{230}Th/^{238}U$) activity ratio**	**±**	**($^{234}U/^{238}U$) activity ratio**	**±**
UEVA246	2a	26.45	0.24	1.1564	0.0025	0.2128	0.0183	1.1519	0.0044
UEVA249	2a	20.02	0.24	1.1421	0.0023	0.1693	0.0111	1.1379	0.0029
UEVA247	2c	91.69	2.80	1.1923	0.0053	0.5293	0.0951	1.2071	0.0421
UEVA248	4a	126.21	1.41	1.2487	0.0033	0.7688	0.0371	1.2283	0.0363

			Corrected results			
Lab ID	**Layer**	**Dated material**	**Age (ka)**	**±**	**$(^{234}U/^{238}U)_{initial}$ activity ratio**	**±**
UEVA246	2a	flowstone	22.20	2.11	1.1617	0.0047
UEVA249	2a	flowstone	17.54	1.25	1.1449	0.0031
UEVA247	2c	flowstone	61.82	14.99	1.2467	0.0491
UEVA248	4a	flowstone	102.98	9.62	1.3055	0.0444

All ratios are activity ratios. Analytical errors are at 95 % confidence level.
Activity ratios are calculated from isotope concentration ratios using decay constants according to *49* (λ238), *50* (λ234 and λ230) and *51* (λ232).
The degree of detrital ^{230}Th contamination is indicated by the measured $^{230}Th/^{232}Th$ activity ratio and corrections were calculated using a $^{238}U/^{232}Th$ activity ratio of 0.8 ± 0.4 and assuming secular equilibrium of the ^{238}U decay chain in the detritus.

Table S3. Uranium-Series results from the Max Planck Institute, Leipzig, Germany.

Lab ID	Layers	Dated material	^{238}U (ng/g)	±	^{232}Th (ng/g)	[$^{230}Th/^{232}Th$] activity ratio
CNESTEN 19-18	4c	animal tooth	1823	145	< 39.27 *	> 125.62
CNESTEN 17-01	2a	animal tooth	3045	180	< 39.27	> 30.71
CNESTEN 17-02	2b	animal tooth	3244	321	< 39.27	> 114.94
CNESTEN 18-13	2c	flowstone	470	38	< 39.27	> 23.26
CNESTEN 18-05	3b	flowstone	492	46	< 39.27	> 23.26
CNESTEN 19-15	4b	animal tooth	2819	222	< 39.27	> 172.50
CNESTEN 20-15	4c'	speleothem	486	25	< 39.27	> 28.36

		Measured ratios							Results	
Lab ID	Layers	($^{232}Th/^{238}U$) activity ratio	($^{230}Th/^{238}U$) activity ratio	±	($^{234}U/^{238}U$) activity ratio	±	($^{230}Th/^{234}U$) activity ratio	±	Age (ka)	±
CNESTEN 19-18	4c	< 0.007	0.89	0.12	1.16	0.13	0.76	0.10	149.15	+63.84/-36.69
CNESTEN 17-01	2a	< 0.004	0.13	0.01	1.04	0.09	0.12	0.01	14.44	+1.54/-1.50
CNESTEN 17-02	2b	< 0.004	0.46	0.06	1.28	0.17	0.36	0.04	47.38	+7.69/-6.91
CNESTEN 18-13	2c	< 0.027	0.64	0.07	1.26	0.14	0.51	0.06	74.56	+13.86/-11.75
CNESTEN 18-05	3b	< 0.026	0.61	0.08	1.05	0.14	0.58	0.05	93.85	+17.44/-13.45
CNESTEN 19-15	4b	< 0.005	0.79	0.08	1.21	0.13	0.65	0.06	110.69	+22.31/-17.25
CNESTEN 20-15	4c'	< 0.026	0.90	0.07	1.20	0.08	0.75	0.06	142.28	+29.30/-22.06

(*) 39.27 ng/g is the Minimum Detectable Concentration (MDC) for ^{232}Th

Table S4. Uranium-Series results from the National Centre for the Techniques Science and Nuclear Energy (CNESTEN), Rabat, Morocco (2-sigma confidence limits).

Sample ID	Layer	n	n_{sat}	OD (%)	D_e (Gy)[1]	WC (%)[2]	Beta dose rate (Gy/ka)[3]	Gamma dose rate (Gy/ka)[3]	Cosmic dose rate (Gy/ka)[4]	Environmental dose rate (Gy/ka)	Age (ka)
L-EVA-1824	3	105	39	26	77.5 ± 2.3	14.2	0.57 ± 0.05	0.33 ± 0.03	0.15 ± 0.02	1.04 ± 0.06	74.6 ± 5.2
L-EVA-1825	3	120	31	23	71.8 ± 1.8	15.1	0.51 ± 0.04	0.30 ± 0.02	0.15 ± 0.02	0.95 ± 0.05	75.3 ± 4.5
L-EVA-1826	3	70	31	47	73.7 ± 4.4	13.8	0.57 ± 0.05	0.35 ± 0.03	0.15 ± 0.02	1.06 ± 0.06	69.4 ± 5.5
L-EVA-1827	3	111	63	26	92.2 ± 2.8	15.7	0.74 ± 0.08	0.41 ± 0.03	0.14 ± 0.01	1.29 ± 0.08	71.3 ± 5.1
L-EVA-1828	3	127	46	30	81.9 ± 2.5	20.5	0.67 ± 0.06	0.39 ± 0.03	0.14 ± 0.01	1.20 ± 0.07	68.2 ± 4.2
L-EVA-1829	3	84	79	24	97.5 ± 3.1	18.5	0.81 ± 0.07	0.46 ± 0.03	0.14 ± 0.01	1.40 ± 0.07	69.4 ± 4.3
L-EVA-1830	4c	93	59	27	95.7 ± 3.1	18.5	0.96 ± 0.08	0.56 ± 0.04	0.14 ± 0.01	1.66 ± 0.09	57.8 ± 3.6
L-EVA-1831	4c	117	46	25	82.8 ± 2.3	15.4	0.78 ± 0.06	0.44 ± 0.03	0.13 ± 0.01	1.35 ± 0.07	61.4 ± 3.7

[1]Representative D_e value calculated using the CentralAge Model (CAM) of Galbraith et al. *(55).*
[2]Water content measured directly from samples after collection.
[3]External beta and gamma dose rates were corrected for grain size attenuation and water attenuation. Water content corrections were made using the measured water content (WC).
[4]Cosmic dose rate inside the cave was estimated from the depth of the overburden, including the thickness of the cave roof.

Table S5. Results of the equivalent dose (D_e) measurements and the dose rate calculations for the single grain quartz ages measured at the Max Planck Institute, including the number of measurements in the dose distribution (n), the number of saturated grains (n_{sat}), the overdispersion (OD) and the equivalent dose (D_e) value used to calculate the age and measured water content (WC).

Lab code	layer	Equivalent dose (Gy)		1 sigma uncertainty	Total dose rate (mGy/yr)		1 sigma uncertainty	Age (ka)		1 sigma uncertainty
Shfd15071	4c (upper)	72.1	±	2.9	0.66	±	0.05	109	±	9
Shfd15072	Disturbed	97.8	±	3.8	1.10	±	0.08	89.1	±	7.4
Shfd15073	2b	38.5	±	1.7	0.86	±	0.06	44.7	±	3.7
Shfd15074	4a	101	±	4.2	1.22	±	0.09	82.7	±	6.9
Shfd15075	3	88.7	±	2.4	1.18	±	0.08	75.0	±	5.7
Shfd19072	4c	95.2	±	4.0	1.23	±	0.09	77.1	±	6.4
Shfd19073	4c	98.2	±	3.3	1.48	±	0.11	66.4	±	5.4
Shfd19074	4c	114	±	5.2	1.53	±	0.11	74.6	±	6.4
Shfd19075	4c	145	±	8.3	1.52	±	0.11	54.3	±	4.7
Shfd19076	4a/b	77.3	±	3.1	0.92	±	0.07	83.9	±	6.9
Shfd19077	3inf	96.3	±	4.4	1.01	±	0.07	95.0	±	8.0

Table S6: Optically Stimulated Luminescence Results, Sheffield University Lab.

REFERENCES AND NOTES

1. D. E. Bar-Yosef Mayer, B. Vandermeersch, O. Bar-Yosef, Shells and ochre in Middle Paleolithic Qafzeh Cave, Israel: Indications for modern behavior. *J. Hum. Evol.* **56**, 307–314 (2009).

2. M. Vanhaeren, D. d'Errico, C. Stringer, S. L. James, J. A. Todd, H. K. Mienis, Middle paleolithic shell beads in Israel and Algeria. *Science* **312**, 1785–1788 (2006).

3. R. Grün, C. Stringer, F. McDermott, R. Nathan, N. Porat, S. Roberts, L. Taylor, G. Mortimer, S. Eggins, M. McCulloch, U-series and ESR analyses of bones and teeth relating to the human burials from Skhul. *J. Hum. Evol.* **49**, 316–334 (2005).

4. C. Henshilwood, F. d'Errico, M. Vanhaeren, K. van Niekerk, Z. Jacobs, Middle Stone Age shell beads from South Africa. *Science* **304**, 404 (2004).

5. Z. Jacobs, E. H. Hayes, R. G. Roberts, R. F. Galbraith, C. S. Henshilwood, An improved OSL chronology for the Still Bay layers at Blombos Cave, South Africa: Further tests of single-grain dating procedures and a re-evaluation of the timing of the Still Bay industry across southern Africa. *J. Archaeol. Sci.* **40**, 579–594 (2013).

6. M. Vanhaeren, L. Wadley, F. D'Errico, Variability in Middle Stone Age symbolic traditions: The marine shell beads from Sibudu Cave, South Africa. *J. Archaeol. Sci. Rep.* **27**, 101893, (2019).

7. A. Bouzouggar, N. Barton, M. Vanhaeren,. F. d'Errico, S. Colcutt, T. Higham, E. Hodge, S. Parfitt, E. Rhodes, J.-L. Schwenninger. C. Stringer, E. Turner, S. Ward, A. Moutmir, A. Stambouli, 82,000-year-old shell beads from North Africa and implications for the origins of modern human behavior. *Proc. Natl. Acad. Sci. U.S.A.* **104**, 9964–9969 (2007).

8. H. L. Dibble, V. Aldeias, E. Álvarez-Fernández, B. A. B. Blackwell, E. Hallett-Desguez, Z. Jacobs, P. Goldberg, S. C. Lin, A. Morala, M. C. Meyer, D. I. Olszewski, K. E. Reed, D. N. Reed, Z. Rezek, D. Richter, R. G. Roberts, D. M. Sandgathe, U. A. Schurmans, A. R. Skinner, T. E. Steele, M. A. El-Hajraoui, New excavations at the site of Contrebandiers Cave, Morocco. *PaleoAnthro.* **2012**, 145–201 (2012).

9. Z. Jacobs, M. C. Meyer, R. G. Roberts, V. Aldeias, H. L. Dibble, M. A. El-Hajraoui, Single-grain OSL dating at La Grotte des Contrebandiers ('Smugglers' Cave), Morocco: Improved age constraints for the Middle Paleolithic levels, *J. Archaeol. Sci.* **38**, 3631–3643 (2011).

10. M. A. El-Hajraoui, H. Oudouche, R. Nespoulet, Etude des coquilles perforées découvertes à Témara, in *Préhistoire de la Région de Rabat-Témara,* M. A. El Hajraoui, R. Nespoulet, A. Debénath, H. L. Dibble, Eds. *V.E.S.A.M.* **III**, 191–199 (2012).

11. N. Janati-Idrissi, C. Falguères, R. Nespoulet, M. A. El Hajraoui, A. Debénath, L. Bejjit, J.-J. Bahain, P. Michel, T. Garcia, L. Boudad, K. El Hammouti, A. Oujaa, Datation par ESR-U/Th combinées de dents fossiles des grottes d'EL Mnasra et d'El Harhoura 2, région de Rabat-Témara. Implications chronologiques sur le peuplement du Maroc atlantique au Pléistocène supérieur et son environnement. *Quaternaire* **23**, 25–35 (2012).

12. D. Richter, J. Moser, M. Nami, J. Eiwanger, A. Mikdad, New chronometric data from Ifri n'Ammar (Morocco) and the chronostratigraphy of the Middle Palaeolithic in the Western Maghreb. *J. Hum. Evol.* **59**, 672–679 (2010).

13. J. Morel, La station éponyme de l'Oued Djebbana à Bir-el-Ater (Est Algérien). *L'Anthropol.* **78**, 53–80 (1974).

14. J. Morel, Nouvelles datations absolues des formations littorales et gisements préhistoriques de l'Est Algérien. *Bull. Soc. Préh. Fr.* **71**,103–105 (1974).

15. A. Bouzouggar, J. Collina-Girard, S. Cravinho, P. Fernandez, A. Gallin, Prospections et sondages sur les littoraux oriental et sud-atlantique du Maroc. *Les nouv. de l'archéol.* **120&121**, 110–116 (2010).

16. M. Fennane, M. Tattou, J. Mathez, A. Ouyahya, J. Oualidi, *Flore Pratique du Maroc* (Institut Scientifique de Rabat, Rabat, 1999).

17. A. Benabid, Bref aperçu sur la zonation altitudinale de la végétation climacique du Maroc. *Ecol. Mediterr.*, **7**, 301–3015 (1982).

18. N. Doerschner, K. E. Fitzsimmons, P. Ditchfield, S. J. McLaren, T. E. Steele, C. Zielhofer, S. P. McPherron, A. Bouzouggar, J.-J. Hublin.,A new chronology for Rhafas, northeast Morocco, spanning the North African Middle Stone Age through to the Neolithic. *PLOS ONE* **11**, e0162280 (2016).

19. R. White, N. Arts, P. G. Bahn, L. R. Binford, M. Dewez, H. L. Dibble, P. R. Fish, C. Gamble, C. Meiklejohn, M. Y. Ohel, J. Pfeiffer, L. G. Straus, T. Weber, Rethinking the Middle/Upper Paleolithic transition [and comments and replies]. *Curr. Anthropol.* **23**,169–192 (1982).

20. S. L. Kuhn, M. C. Stiner, D. S. Reese, E. Güleç, Ornaments of the earliest Upper Paleolithic: New insights from the Levant. *Proc. Natl. Acad. Sci. U.S.A.* **98**, 7641–7646 (2001).

21. A. S. Brooks, J. E. Yellen, R. Potts, A. K. Behrensmeyer, A. L. Deino. D. E. Leslie, S. H. Ambrose, J. R. Ferguson, F. d'Errico, A. M. Zipkin, S. Whittaker, J. Post, E. G. Veatch, K. Foecke, J. B. Clark, Long-distance stone transport and pigment use in the earliest Middle Stone Age. *Science* **360**, 90–94 (2018).

22. T. Steele, E. Álavarez-Fernández, E. Hallett-Desguez, A review of shells as personal ornamentation during the African Middle Stone Age. *PaleoAnthro* **2019**, 24–51 (2019).

23. M. Stiner, Finding a common bandwidth: Causes of convergence and diversity in Paleolithic beads. *Biol. Theor.* **9**, 51–64 (2014).

24. D. Richter, R. Grün, R. Joannes-Boyau, T. E. Steele, F. Amani, M. Rué, P. Fernandes, J.-P. Raynal, D. Geraads, A. Ben-Ncer, J.-J. Hublin, S. P. McPherron, The age of the hominin fossils from Jebel Irhoud, Morocco, and the origins of the Middle Stone Age. *Nature* **546**, 293–296 (2017).

25. A. Bouzouggar , L. T. Humphrey, N. Barton, S. A. Parfitt, L. Clark Balzan, J.-L. Schwenninger, M. A. El Hajraoui, R. Nespoulet, S. M. Bello, 90,000 year-old specialised bone technology in the Aterian Middle Stone Age of North Africa. *PLOS ONE* **3**, e0202021 (2018).

26. E. M. L. Scerri, M. G. Thomas, A. Manica, P. Gunz, J. T. Stock, C. Stringer, M. Grove, H. S. Groucutt. A. Timmermann, G. P. Rightmire, F. d'Errico, C. A. Tryon, N. A. Drake, A. S. Brooks, R. W. Dennell, R. Durbin, B. M. Henn, J. Lee-Thorp, P. deMenocal, M. D. Petraglia, J. C. Thompson,

A. Scally, L. Chikhi, Did our species evolve in subdivided populations across Africa, and why does it matter? *Tr. Ecol. Evol.* **33**, 582–594 (2018).

27. M. M. Haaland, M. Czechowski, F. Carpentier, M. Lejay, B. Vandermeulen, Documenting archaeological thin sections in high-resolution: A comparison of methods and discussion of applications. *Geoarchaeology* **34**, 100–114 (2019).

28. B. Lafuente, R. T. Downs, H. Yang, N. Stone, The power of databases: The RRUFF project, in *Highlights in Mineralogical Crystallography*, T. Armbruster, R. M Danisi, Eds. (Berlin, W. De Gruyter, 2016), pp 1–30.

29. F. d'Errico, M. Vanhaeren, N. Barton, A. Bouzouggar, H. Mienis, D. Richter, J.-J. Hublin, S. P. McPherron, P. Lozouet, Additional evidence on the use of personal ornaments in the Middle Paleolithic of North Africa. *Proc. Natl. Acad. Sci. U.S.A.* **106**, 16051–16056 (2009).

30. M. Hafid, Triassic–early Liassic extensional systems and their Tertiary inversion, Essaouira Basin (Morocco). *Mar. Pet. Geol.* **17**, 409–429 (2000).

31. X. S. Villagran, D. J. Huisman, S. M. Mentzer, C. E. Miller, M. M. Jans, Bone and other skeletal tissues, in *Archaeological Soil and Sediment Micromorphology*, C. Nicosia, G. Stoops, Eds. (Wiley, 2017), pp. 11–38.

32. J. Petit, J. Jouzel, D. Raynaud, N. I. Barkov, J.-M. Barnola, I. Basile, M. Bender, J. Chapellaz, M. Davis, G. Delaygue, M. Delmotte, V. M. Kotlyakov, M. Legrand, V. Y. Lipenkov, C. Lorius, L. Pépin, E. Saltzman, M. Stievenard, Climate and atmospheric history of the past 420,000 years from the Vostok ice core, Antarctica. *Nature* **399**, 429–436 (1999).

33. B. Ouchaou, B. Bougariane, S. Zahid, De quelques grands mammifères sporadiques dans les sites archéologiques du Pléistocène terminal-Holocène du Maroc. *J. Mat. Envir. Sci.* **7**, 3667–3677 (2015).

34. B. Ouchaou, F. Amani, Etude préliminaire des grands mammifères du gisement de Kaf-Taht-el Ghar (Tetouan, Maroc). *Préhist. Anthropol. Méditerr.*, **6**, 53–60 (1997).

35. B. Bagtache, D. Hadjouis, V. Eisenmann, Présence d'un *Equus* caballin (*E. algericus* sp.) et d'une autre espèce nouvelle d'*Equus* (*E. melkiensis* sp.) dans l'Atérien des Allobroges, Algérie. *C. Rend. Acad. Sci. Paris*, série II, **298**, 609–612 (1984).

36. H. Aouraghe, A. Debénath, Les équidés du Pléistocène supérieur de la grotte Zouhrah à El Harhoura, Maroc [The equidae from upper Pleistocene of Zouhrah cave of El Harhoura, Morocco]. *Quaternaire* **10**, 283–292 (1999).

37. H. Aouraghe, Les populations de mammifères atériens d'El Harhoura 1 (Témara, Maroc). *Bull. Archéol. Maroc.* **20**, 83–10 (2004).

38. P. Michel, "Contribution à l'étude paléontologique des vertébrés fossiles du Quaternaire marocain à partir de sites du Maroc atlantique, central et oriental," thesis, Muséum National d'Histoire Naturelle de Paris, Institut de Paléontologie Humaine (1990).

39. D. Geraads, The faunal context of human evolution in the late Middle / Late Pleistocene of North-western Africa, in *Modern Origins: A North African Perspective*, J.-J. Hublin, S. P. McPheron, Eds. (Springer, Dordrecht, 2012), pp. 49–60.

40. D. Geraads, "Grands Mammifères fossiles du Maroc", in *Mammifères Sauvages du Maroc. Peuplement, Répartition, Écologie*, S. Aulagnier, F. Cuzin, M. Thévenot, Eds. S.F.E.P.M., pp. 63–72 (2017).

41. P. Michel, L. Wengler, Un site paléontologique avec des vestiges archéologiques : la carrière Doukkala II (Région de Temara, Maroc atlantique), Paléoécologie des faunes et contribution à la connaissance du comportement humain. *Paléo*, **5**, 11–41 (1993).

42. P. Fernandez, A. Bouzouggar, J. Collina-Girard, M. Coulon, The last occurrence of *Megaceroides algericus* Lyddekker, 1890 (Mammalia, Cervidae) during the middle Holocene in the cave of Bizmoune (Morocco, Essaouira region). *Quat. Int.* **374**, 154–167 (2015).

43. B. Ouchaou, F. Amani, Les Carnivores des gisements néolithiques et protohistoriques du Nord du Maroc / The neolithic and protohistoric camivorafrom northern Morocco. *Quaternaire* **13**, 79–87 (2002).

44. A. Benabid, Etude phytoécologique des peuplements forestiers et préforestiers du Rif centro-occidental (Maroc). *Trav. Inst. Sc., Sb. Bot.* **34**, 64 p (1984).

45. F. d'Errico, A. P. Martía, C. Shipton, E. Le Vraux, E.Ndiema, S.Goldstein, M. D. Petraglia, N. Boivin. Trajectories of cultural innovation from the Middle to Later Stone Age in Eastern Africa: Personal ornaments, bone artifacts, and ocher from Panga ya Saidi, Kenya. *J. Hum. Evol.* **141**, 102737 (2020).

46. D. Bar-Yosef Mayer, I. Groman-Yaroslavski, O. Bar-Yosef, I. Hershkovitz, A. Kampen-Hasday, B. Vandermeersch, Y. Zaidner, M. Weinstein-Evron, On holes and strings: Earliest displays of human adornment in the Middle Palaeolithic. *PLOS ONE* **15**, e0234924 (2020).

47. World Register of Marine Species, *Nassarius gibbosulus* (Linnaeus, 1758). Mollusca Base (2019); www.marinespecies.org/aphia.php?p=taxdetails&id=140499

48. M. Oliverio, L. Tringali, Two sibling species of Nassariinae in the Mediterranean Sea (Prosobranchia, Muricidae, Nassariinae). *Boll. Malacol.* **28**, 157–160 (1992).

49. A. H. Jaffey, K. F. Flynn, L. E. Glendenin, W. C. Bentley, A. M. Essling, Precision measurement of half-lives and specific activities of U235 and U238. *Phys. Rev. C* **4**, 1889–1906 (1971).

50. H. R. Cheng, R.L Edwards, J. Hoff, C.D Gallup, D. A. Richards, Y. Asmerom, The half-lives of uranium-234 and thorium-230. *Chem. Geol.* **169**, 17–33 (2000).

51. N. E. Holden, Total half-lives for selected nuclides. *Pure Appl. Chem.* **62**, 941–958 (1990).

52. J. L. Bischoff, J. A. Fitzpatrick, U-series dating of impure carbonates: An isochron technique using total-sample dissolution. *Geochim. Cosmochim. Acta* **55**, 543–554 (1991).

53. A. Martinez-Aguirre, J. M. Alcaraz-Pelegrina, U/Th dating of impure carbonates: $^{230}Th/^{232}Th$ activity ratios in detrital material. *J. Radioanal. Nucl. Chem.*, **321**, 71–81 (2019).

54. G. A. T. Duller, Distinguishing quartz and feldspar in single grain luminescence measurements. *Radiat. Meas.* **37**, 161–165 (2003).

55. R. F. Galbraith, R. G. Roberts, G. M. Laslett, H. Yoshida, J. M. Olley, Optical dating of single and multiple grains of quartz from Jinmium rock shelter, northern Australia: Part I, experimental design and statistical models. *Archaeometry* **41**, 339–364 (1999).

56. J. A. Durcan, G. A. King, G. A. T. Duller, DRAC: Dose rate and age calculator for trapped charge dating. *Quat. Geochronol.* **28**, 54–61 (2015).

57. E. J. Rhodes, Dating sediments using potassium feldspar single-grain IRSL: Initial methodological considerations. *Quat. Int.* **362**, 14–22 (2015).